

Optimal Current Allocation Rendering 3-D Magnetic Force Production in Hexapole Electromagnetic Actuation

Fei Long^{ID}, Peng Cheng^{ID}, Ta-Min Meng^{ID}, and Chia-Hsiang Menq^{ID}

Abstract—This article presents the optimal current allocation and the magnetic force production associated with the hexapole electromagnetic actuation, wherein six electromagnets are used to control the magnetic field and exert the 3-D magnetic force on a specified microscopic magnetic particle in the 3-D workspace of the actuating system. It addresses four major issues in the inverse modeling of the multipole electromagnetic actuation, i.e., 1) redundancy; 2) coupling; 3) nonlinearity; and 4) position-dependency, and leads to the accurate and effective 3-D magnetic force production within the specified workspace. Specifically, the optimal inverse modeling of the hexapole electromagnetic actuation is derived to minimize the 2-norm of the 6×1 input current vector when applied to produce the desired 3-D magnetic force to propel the magnetic particle in aqueous solutions. The inverse model is implemented in a high-speed field programmable gate array system to realize the real-time current allocation, which is used to render the feedback stabilization of the magnetic trap. The accurate and effective 3-D force production through the optimal current allocation is experimentally validated.

Index Terms—Current allocation, electromagnetic actuation, inverse modeling, motion control.

I. INTRODUCTION

LECTROMAGNETIC actuating systems use electromagnets to control the magnetic field and exert the controllable magnetic force on microscopic magnetic objects. They have led to the development of modern instruments that enable advanced techniques employed in biomedical research. With precalibrated force functions, some were used as force applicators to manipulate biological macromolecules [1]–[3] or magnetic particles [4], [5], to probe cell membranes [6]–[8], or to characterize

Manuscript received June 8, 2020; revised August 17, 2020 and October 5, 2020; accepted November 16, 2020. Date of publication November 19, 2020; date of current version October 14, 2021. Recommended by Technical Editor X. Zhang and Senior Editor Y. Li. (Corresponding author: Chia-Hsiang Menq.)

Fei Long was with the Ohio State University, Columbus, OH 43210 USA. He is now a staff engineer at UBTECH Robotics North America Research and Development Center, Pasadena, CA 91101 USA (e-mail: long.926@osu.edu).

Peng Cheng, Ta-Min Meng, and Chia-Hsiang Menq are with the Department of Mechanical and Aerospace Engineering, The Ohio State University, Columbus, OH 43210 USA (e-mail: cheng.329@osu.edu; meng.350@osu.edu; menq.1@osu.edu).

Color versions of one or more of the figures in this article are available online at <https://doi.org/10.1109/TMECH.2020.3039258>.

Digital Object Identifier 10.1109/TMECH.2020.3039258

intracellular properties [9]–[12]. Some others were employed to propel microscopic robots as swimming machines [13]–[15] or for medical applications [16], [17].

More recently, overactuated multipole actuating systems, e.g., 2-D quadrupole magnetic tweezers [18] and 3-D hexapole electromagnetic actuators [19], were developed. The hexapole actuator employed six sharp-tipped electromagnetic poles, made of thin high-permeability nickel-iron magnetic alloy film, and six actuating coils to achieve the 3-D electromagnetic actuation. Due to the inherent instability of the magnetic force field when applied to exert force on a magnetic particle [20], the real-time 3-D visual tracking was realized to enable the particle tracking and visual servo control, running at 200 Hz with nanometer resolution [21]. The acquired particle motion was then used in the feedback control laws, designed to adjust actuating currents and thus alter the field potential, to trap and steer a microscopic magnetic particle in aqueous solutions [22], [23]. The magnetic particle was employed to serve as a measurement probe, which was steered to interact with live cells in media to characterize their mechanical properties [24].

Multipole electromagnetic actuators are overactuated and strongly coupled nonlinear systems, wherein the number of input currents is greater than that of output force components, and the resulting magnetic force field is nonlinearly related to the input currents and has strong spatial heterogeneity. The capability and performance of these actuators rely on the accurate and effective inverse modeling of the multipole electromagnetic actuation, which is essential for the superior current allocation and active feedback control.

While stable magnetic trapping and motion control were successfully demonstrated [22], [23], the simplification adopted in inverse modeling severely limited the performance of the developed actuating systems on two fronts. First, constant constraints are used to remove redundancies to derive the simple inverse model, which is valid at the center of the workspace, resulting in the excessive current flow in the coil. It significantly degrades the force generation capability of the actuating system. Second, extending the inverse model at the center to the entire workspace through the linear approximation in the spatial domain leads to significant errors when generating the magnetic force exerting on the magnetic particle placed away from the center of the workspace.

This article presents the optimal inverse modeling to enable the real-time current allocation in the multipole electromagnetic

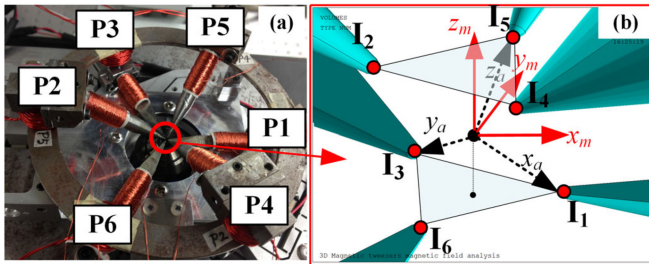


Fig. 1. Hexapole electromagnetic actuator. (a) Arrangement of the six electromagnetic poles. (b) Measurement coordinate $\{x_m, y_m, z_m\}$ and actuation coordinate $\{x_a, y_a, z_a\}$ associated with the six pole tips.

actuation. A hexapole electromagnetic actuating system is used as a model system to investigate the mathematical relationship between the desired 3-D magnetic force exerting on the magnetic particle and the six required input currents. It also serves as an experimental platform to demonstrate the effective 3-D magnetic force production as the hexapole actuating system being used to achieve stable magnetic trapping.

The rest of this article is organized as follows. Section II presents the experimental apparatus, including the hexapole electromagnetic actuating system [25], the 3-D particle tracking system, and the field programmable gate array (FPGA) based real-time implementation. Section III presents the inverse modeling and the optimal current allocation. Experimental investigations of the effective 3-D force production through the optimal current allocation are presented in Section IV, wherein the hexapole system is used to achieve the magnetic trapping and motion control. Experimental results associated with the actuation current, the Brownian motion [26], [27], and the positioning and tracking error are also discussed. Finally, Section V concludes this article.

II. EXPERIMENTAL APPARATUS

The experimental apparatus is a magnetic particle trapping system, consisting of a hexapole actuating system, a 3-D particle tracking system, and a real-time control system.

A. Hexapole Electromagnetic Actuating System

The system is designed for use with live cell experiments. It employs six sharp-tipped electromagnetic poles, made of cone-shaped 1018 steel rod (0.18% carbon) steel with a high saturation limit (over 2 T). All the poles are magnetically connected through a magnetic yoke. Each pole is actuated using an individual coil, having 70 turns with the current limitation being 3 A. The distance from the workspace center to the tips of all six poles is adjustable due to the flexibility achieved in the design. Its nominal value of 500 μm is used in all analyses and experiments reported in this article. With the design [25], the magnitude of the resulting magnetic flux density at the center of the workspace is about 100 Gauss (0.01 T) when applying 1-A current to one of the six poles.

Fig. 1(a) shows the top view of the hexapole magnetic actuator. The six poles are arranged in a 3-D configuration such

that their tips enclose the workspace, wherein the specimen cells and the magnetic particle are placed. Two coordinate systems, i.e., the measurement coordinate and actuation coordinate, are defined for the purpose of measurement and of actuation modeling, respectively. They are shown in Fig. 1(b). The z -axis of the measurement coordinate is aligned to the optical axis of the microscope employed for the particle tracking. Three pairs of electromagnetic poles are aligned along the three orthogonal axes of the actuation coordinate. Through a rigid body rotation, tips of the six poles are on two parallel horizontal planes in the measurement coordinate, i.e., one upper plane and the other lower plane, and the blockage of the optical path is avoided.

The pole tips are used to concentrate the magnetic flux into the workspace to generate and control the magnetic field and exert the controllable magnetic force on the magnetic particle. The resulting magnetic field can be obtained by summing the magnetic field contributed by each individual pole. Fig. 1(b) shows the association between the six pole tips and six input currents, wherein I_2 , I_4 , and I_5 are associated with the three upper poles and I_1 , I_3 , and I_6 with the three lower poles. Without being magnetized to saturation, the 3-D magnetic force exerted on a superparamagnetic microscopic particle placed in the field is described by the gradient force $\mathbf{F} = (\frac{1}{2})\nabla(\mathbf{m} \cdot \mathbf{B})$, where \mathbf{B} is the vector of the resulting magnetic flux density at the particle's location, denoted as \mathbf{p} , and \mathbf{m} the effective magnetization of the magnetic particle. The gradient force produced by the six input currents, denoted as \mathbf{I} , can be cast into a quadratic form [25]

$$\mathbf{F}(\mathbf{p}, \mathbf{I}) = g_I I_{\max}^2 \hat{\mathbf{I}} \mathbf{K}_I^T \mathbf{L}(\hat{\mathbf{p}}) \mathbf{K}_I \hat{\mathbf{I}} = g_I I_{\max}^2 \hat{\mathbf{F}}(\hat{\mathbf{p}}, \hat{\mathbf{I}}) \quad (1)$$

where $\hat{\mathbf{p}}$ is the position vector normalized with respect to the effective workspace radius ℓ , $\hat{\mathbf{I}}$ the normalized current vector, i.e., $\hat{\mathbf{I}} = \mathbf{I}/I_{\max}$, and I_{\max} the maximum current specified for the safety operation. The 6×6 symmetric flux distribution matrix \mathbf{K}_I could be determined through three distinct approaches: 1) magnetic circuit analysis [19]; 2) finite-element analysis [25]; and 3) experimental calibration [25]. The distance from the workspace center to the tips of all six poles is adjustable, i.e., between 200 and 1000 μm . The effective workspace radius, however, needs to be determined through either the second or the third approach. Nonetheless, associated with the design of the hexapole actuating system, $\mathbf{L}(\hat{\mathbf{p}})$ is known. It characterizes the position-dependency of the 3-D magnetic force experienced by the magnetic particle in the normalized workspace. It is worth noting that the three components of the force, presented in [25], are combined into a single vector in (1). Therefore, $\mathbf{L}(\hat{\mathbf{p}})$ consists of three 6×6 matrices. The force gain, i.e., g_I , is characterized by the size and magnetic property of the magnetic particle and that of the magnetic circuit. It is often determined through the experimental calibration [25].

It is evident that $g_I I_{\max}^2$ in (1) determines the force generation capability of the actuating system, whereas the dimensionless force field, i.e., $\hat{\mathbf{F}}(\hat{\mathbf{p}}, \hat{\mathbf{I}})$, characterizes the nonlinearity, coupling, position-dependence, and redundancy of the hexapole electromagnetic actuation.

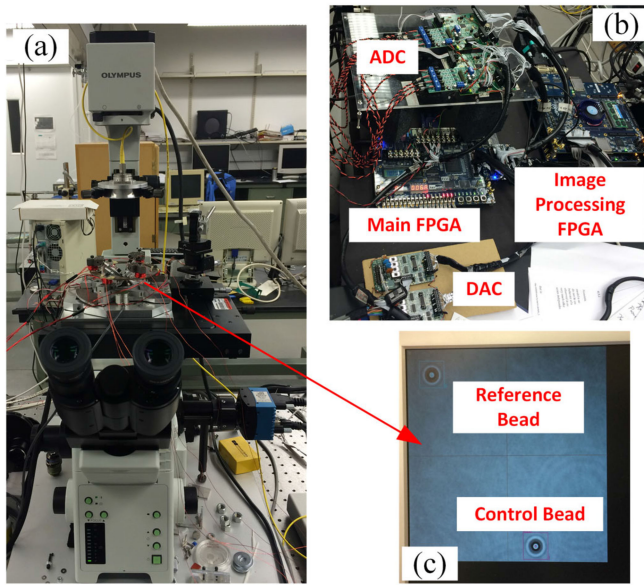


Fig. 2. (a) Hexapole actuator integrated with an inverted microscope. (b) FPGA-based controller and real-time image processor. (c) Real-time image display of the reference bead and the control bead.

B. 3-D Particle Tracking System

A real-time system achieving the high-speed 3-D particle tracking with nanometer resolution was reported in [28]. This system has been implemented with two major improvements in this study to track the 3-D motion of the magnetic particle in aqueous solutions with subnanometer resolution. It comprises a complementary metal-oxide-semiconductor (CMOS) camera, an FPGA, and real-time image processing programs. As shown in Fig. 2(a), the hexapole electromagnetic actuator is integrated upon an inverted microscope (Olympus IX81) and the CMOS camera is used to grab images for real-time motion tracking.

The CMOS camera has high photosensitivity and superior signal-to-noise ratio. In the new experimental setup, a super luminescent diode (SLD) illumination system instead of a standard 100-W halogen lamp is used to further enhance the image sensitivity [29]. The vision system is, therefore, able to acquire images of 256×120 pixels at a frame rate of up to 10 000 frames per second (fps). Since the SLD has a long coherence length, an enhanced diffraction pattern can be generated, improving the measurement resolution in both the lateral direction and axial direction.

The real-time image stream is downloaded to the FPGA [Fig. 2(b)], wherein a 3-D particle-tracking algorithm is implemented to calculate the 3-D positions of the particle in real time. Upon receiving each incoming image, the second improvement is to use the continuous image registration method [30] to determine the lateral position of the spherical particle, and an optimal matching technique [31] is employed to compare the off-focus 2-D image with an object-specific model to estimate the axial position. The achieved optical resolution is about 0.003 pixels in the x - and y -directions, and sub-nm in the z -direction. The CMOS camera used in this system has 8- μm pixel size. Therefore, the visual sensing resolution is about 0.4 nm in the x -

and y -directions when a $60\times$ lens is used and 0.6 nm when a $40\times$ lens is used. Two important objectives are achieved. First, the real-time estimation of the 3-D position matches the maximum frame rate of the camera. Second, the timing of the output data stream of the system is precisely controlled.

C. Real-Time Control System

A DE2-115 FPGA (Terasic Inc.) is used as the main FPGA to implement the developed control algorithms, wherein the six desired control currents are calculated. The six control signals are sent to six linear power amplifiers (Micro Dynamics, BTA-28V-6A) through DA converters (DAC8814 EVM, Texas Instruments) to generate control currents to actuate individual coils. A dual-bead tracking system is implemented using two TR4-230 FPGAs (Terasic Inc.), in which the real-time image processing is performed to calculate the respective positions of two magnetic beads, namely the reference bead and the control bead, associated with each incoming image frame. The integration of the image processing FPGA with the main FPGA is shown in Fig. 2(b), wherein the necessary position feedback is provided to the real-time control algorithms through the real-time image processing. The connections of USB modules (DLP-USB1232H, FTDI) are established and programmed to realize the PC-FPGA communication, rendering control parameters downloading. A VGA port of the main FPGA is connected to a monitor to display the image in real time. Fig. 2(c) shows a snapshot of the monitor, displaying the dual-bead tracking, wherein the reference bead is affixed to the coverslip surface and measured simultaneously along with the bead moving in the 3-D workspace. The dual-bead tracking approach enables the drift compensation and the low frequency vibration cancelation. Since a larger region of interest, i.e., 512×512 pixels, is needed for the dual-bead approach, the maximum achievable sampling rate used in the real-time control is 1606 Hz.

III. OPTIMAL CURRENT ALLOCATION

The force model is then used in the inverse modeling to render the optimal current allocation of the overactuated hexapole electromagnetic actuating system, minimizing the 2-norm of the input current vector when applied to produce the desired 3-D magnetic force in the workspace. The optimal current allocation is then realized in real time to enable the feedback linearization. The stable magnetic trapping and precise motion control of the microscopic magnetic particle in the fluid environment are demonstrated in experiments.

A. Current Allocation Based on Constant Constraints

An inverse model based on constant constraints was proposed in [23] to remove redundancies. It is briefly summarized here. The normalized force, i.e., (1), can be significantly simplified at the center of the workspace due to the symmetrical configuration

of the magnetic poles in the actuation coordinate frame

$$\begin{cases} \hat{F}_x(0, \hat{\mathbf{I}}) = 2(\hat{I}_1 - \hat{I}_2)[2(\hat{I}_1 + \hat{I}_2) - (\hat{I}_3 + \hat{I}_4) - (\hat{I}_5 + \hat{I}_6)] \\ \hat{F}_y(0, \hat{\mathbf{I}}) = 2(\hat{I}_3 - \hat{I}_4)[2(\hat{I}_3 + \hat{I}_4) - (\hat{I}_1 + \hat{I}_2) - (\hat{I}_5 + \hat{I}_6)] \\ \hat{F}_z(0, \hat{\mathbf{I}}) = 2(\hat{I}_5 - \hat{I}_6)[2(\hat{I}_5 + \hat{I}_6) - (\hat{I}_1 + \hat{I}_2) - (\hat{I}_3 + \hat{I}_4)] \end{cases}. \quad (2)$$

Letting $\delta\hat{\mathbf{I}} = [\delta\hat{I}_x, \delta\hat{I}_y, \delta\hat{I}_z]^T = [\hat{I}_1 - \hat{I}_2, \hat{I}_3 - \hat{I}_4, \hat{I}_5 - \hat{I}_6]^T$ as effective actuation currents and employing three linear constraints, i.e., $\mathbf{c} = [c_x, c_y, c_z]^T = [\hat{I}_1 + \hat{I}_2, \hat{I}_3 + \hat{I}_4, \hat{I}_5 + \hat{I}_6]^T$, to remove redundancies, an exact linear relationship between the effective actuation current and the force is derived

$$\hat{\mathbf{F}}(0, \delta\hat{\mathbf{I}}) = \mathbf{J}_{\delta\hat{\mathbf{I}}} \delta\hat{\mathbf{I}} = 2\mathbf{J}\delta\hat{\mathbf{I}} \quad (3)$$

where $\mathbf{J} = 3 \cdot \text{diag}[c_x, c_y, c_z] - (c_x + c_y + c_z) \cdot \text{diag}[1, 1, 1]$. The effective actuation current $\delta\hat{\mathbf{I}}$ can, therefore, be analytically determined when the bead is at the workspace center. While it is not straightforward to obtain the exact inverse solution for the entire workspace, by keeping the first-order terms in Taylor expansion of (1), a linear approximation of the magnetic force around the center can be cast as $\hat{\mathbf{F}}(\hat{\mathbf{p}}, \delta\hat{\mathbf{I}}) \approx \mathbf{J}_{\delta\hat{\mathbf{I}}} \delta\hat{\mathbf{I}} + \mathbf{J}_{\hat{\mathbf{p}}}\hat{\mathbf{p}}$, wherein $\mathbf{J}_{\hat{\mathbf{p}}} = 2 \cdot \mathbf{J}^2$. The effective actuation current required to produce the desired force is then derived

$$\delta\hat{\mathbf{I}} \approx \frac{1}{2}\mathbf{J}^{-1}\hat{\mathbf{F}}_d(\hat{\mathbf{p}}) - \mathbf{J}\hat{\mathbf{p}}. \quad (4)$$

The effective actuation current $\delta\hat{\mathbf{I}}$ along with the three linear constraints can be employed to calculate the required actuation current, i.e.

$$\mathbf{I} = \text{Inverse}(\mathbf{F}_d, \mathbf{p}, \mathbf{c}). \quad (5)$$

It is worth noting that the desired force \mathbf{F}_d and the spatial location \mathbf{p} are associated with the actuation coordinate frame. While employing (5) to realize the inverse model calculation, the rotational matrix m_R between the two coordinate frames needs to be applied to both vectors.

B. Current Allocation Through Optimization

As shown in (1), the resulting magnetic force nonlinearly relates to the six input currents and strongly depends on the position of the magnetic bead. Employing (5) to allocate the six input currents has two severe limitations that degrade the desired capability of the actuating system. First, whereas the use of constant constraints leads to a simple and accurate inverse model at the center, it results in excessive current flow in the coil and significantly degrades the force generation capability of the actuating system. Second, extending the inverse model at the center to the entire workspace through the first-order Taylor expansion in the spatial domain leads to significant errors when generating the magnetic force exerting on the magnetic particle placed away from the center of the workspace.

It is, therefore, desirable to devise an approach that renders the optimal current allocation, wherein the inverse modeling is accurate within the specified workspace and the 2-norm of the six input currents is minimized. Minimizing the 2-norm of

the six currents while generating the accurate 3-D magnetic force is essentially an optimization problem under nonlinear equality constraints. From (1), due to the quadratic relationship between the magnetic force and the input currents, i.e., $\|\hat{\mathbf{F}}(\hat{\mathbf{p}}, \hat{\mathbf{I}})\| \propto \|\hat{\mathbf{I}}\|^2$, expressing the desired force in magnitude and direction, i.e., $\hat{\mathbf{F}}_d = \|\hat{\mathbf{F}}_d\| \hat{\mathbf{r}}(\varphi, \theta)$ at the specified position $\hat{\mathbf{p}}$, leads to a scalable optimal inverse solution, i.e.

$$\hat{\mathbf{I}}_{\text{opt}}(\hat{\mathbf{F}}_d, \hat{\mathbf{p}}) = \|\hat{\mathbf{F}}_d\|^{1/2} \hat{\mathbf{I}}_{\text{opt}}(\hat{\mathbf{r}}(\varphi, \theta), \hat{\mathbf{p}}) \quad (6)$$

where $\hat{\mathbf{r}}(\varphi, \theta)$ is the unit desired force represented as an unit radial vector in the spherical coordinate system. This scalable relationship allows one to focus only on the direction, not the magnitude, of the desired force when finding the optimal current allocation. Therefore, the objective of optimization is to minimize the 2-norm of the 6×1 input current vector, namely $\|\hat{\mathbf{I}}\|^2$, that produces the desired unit force, i.e., $\hat{\mathbf{r}}(\varphi, \theta) = \hat{\mathbf{I}}^T \mathbf{N}(\hat{\mathbf{p}}) \hat{\mathbf{I}}$. The method of Lagrange multipliers is employed to minimize the objective function subject to equality constraints [32]. Specifically, Lagrange multipliers $\lambda^T = [\lambda_x, \lambda_y, \lambda_z]$ are used to construct the following Lagrange function:

$$\mathcal{L}(\varphi, \theta, \hat{\mathbf{p}}) = \|\hat{\mathbf{I}}\|^2 + \lambda^T (\hat{\mathbf{I}}^T \mathbf{N}(\hat{\mathbf{p}}) \hat{\mathbf{I}} - \hat{\mathbf{r}}(\varphi, \theta)) \quad (7)$$

wherein $\hat{\mathbf{I}}^T \mathbf{N}(\hat{\mathbf{p}}) \hat{\mathbf{I}} - \hat{\mathbf{r}}(\varphi, \theta) = 0$ are three equality constraints and $\|\hat{\mathbf{I}}\|^2$ the objective function.

The use of the Lagrange function converts the constrained problem into a form such that the derivative test can be applied. At a given position of the magnetic bead, minimizing $\|\hat{\mathbf{I}}\|^2$ in (7) yields the optimal inverse solution, represented by $\hat{\mathbf{I}}_{\text{opt}}^{\text{unit}}(\varphi, \theta, \hat{\mathbf{p}})$ and associated with the unit force, i.e., $\hat{\mathbf{F}}_d = \hat{\mathbf{r}}(\varphi, \theta, \hat{\mathbf{p}})$.

The inverse solution is exact within the specified workspace as nonlinear equality constraints, i.e., $\hat{\mathbf{r}}(\varphi, \theta) = \hat{\mathbf{I}}^T \mathbf{N}(\hat{\mathbf{p}}) \hat{\mathbf{I}}$, are satisfied. Moreover, the 2-norm of the input current vector is minimum as the objective function is minimized. To illustrate the importance of the optimal current allocation, two limitations of previous approaches [23], [25] are presented below.

First, the excessive input current attributed to the use of constant constraints is illustrated. For simplicity, the force production at the center of the workspace is examined. At the center, since the inverse solution associated with the three constraints (\mathbf{c}) is known, i.e., $\hat{\mathbf{p}} = 0$ in (4), the optimal current can be obtained by finding three optimal constraints, i.e., $\mathbf{c}(\varphi, \theta)$, that minimize the 2-norm of the input current vector, i.e., $\|\hat{\mathbf{I}}(\varphi, \theta)\|^2$. Since $\delta\hat{\mathbf{I}} = [\hat{I}_1 - \hat{I}_2, \hat{I}_3 - \hat{I}_4, \hat{I}_5 - \hat{I}_6]^T$ and $\mathbf{c} = [\hat{I}_1 + \hat{I}_2, \hat{I}_3 + \hat{I}_4, \hat{I}_5 + \hat{I}_6]^T$, the squared norm of the input current vector is related to the effective input current vector and three constraints as

$$\|\hat{\mathbf{I}}(\varphi, \theta)\|^2 = \frac{1}{2} \left\{ \|\delta\hat{\mathbf{I}}(\varphi, \theta)\|^2 + \|\mathbf{c}\|^2 \right\} \quad (8)$$

where $\delta\hat{\mathbf{I}}(\varphi, \theta) = \frac{1}{2}\mathbf{J}^{-1}\hat{\mathbf{r}}(\varphi, \theta)$ according to (3). The objective function can then be cast as

$$J(\mathbf{c}, \varphi, \theta) = \frac{1}{8} \|\mathbf{J}^{-1}\hat{\mathbf{r}}(\varphi, \theta)\|^2 + \frac{1}{2} \|\mathbf{c}\|^2 \quad (9)$$

which involves three variables, significantly less complicated when compared to the one in (7).

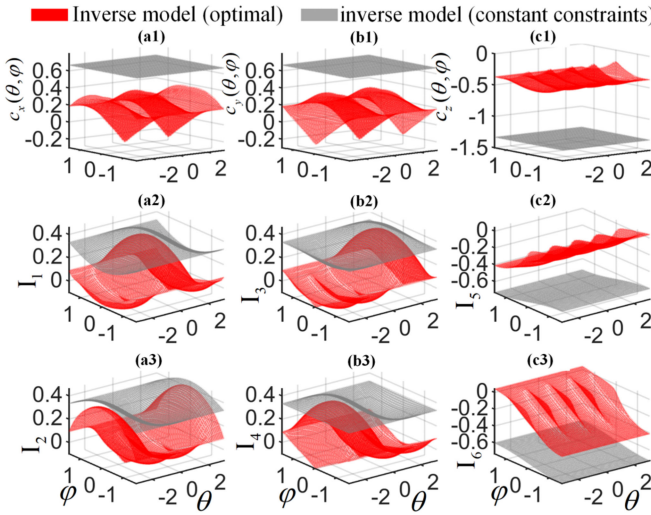


Fig. 3. Three direction-dependent optimal constraints (first row) and optimal allocation of six direction-dependent input currents (second and third rows) compared with their corresponding results using constant constraints.

Minimizing this objective function yields the three direction-dependent optimal constraints $c(\varphi, \theta)$. Employing the optimal constraints, i.e., $c(\varphi, \theta)$, the optimal current allocation, $\hat{\mathbf{I}}_{\text{opt}}^{\text{unit}}(\varphi, \theta)$, associated with the unit force, is then determined. Whereas it only provides the optimal current allocation at the center of the workspace and needs to be extended to the entire workspace using (7), its result showcases that using optimization offers significant advantages over constant constraints used in [19] and [23]. They are displayed in Fig. 3, reproduced from [25, Figs. 7 and 8], wherein the six input currents through the optimal current allocation are much smaller than those obtained using constant constraints.

Second, whereas the inverse model is exact at the center of the workspace, extending from the center through the first-order Taylor expansion, i.e., (5), leads to a significant error as the ability of the force production strongly depends on the position of the bead as shown in (1). Fig. 4 shows the error of the inverse modeling when employing (5) to allocate the input current. It shows that the error grows when moving the bead away from the center (from center to 20 μm and then 40 μm in the x -direction) and/or increasing the desired force (from 1 to 10).

C. Optimal Inverse Model for Real-Time Control

Minimizing $J(\varphi, \theta, \hat{\mathbf{p}})$ in (7) to obtain the position-dependent optimal current allocation, denoted as $\hat{\mathbf{I}}_{\text{opt}}^{\text{unit}}(\varphi, \theta, \hat{\mathbf{p}})$, involves nine variables, i.e., six currents and three Lagrange multipliers. The local minimum occurs at $\nabla(J(\varphi, \theta, \hat{\mathbf{p}})) = 0$, still a nonlinear function. Although the solution removes the error attributed to the first-order Taylor approximation, it is not feasible to be implemented for real-time control.

Two approaches are introduced here to achieve the inverse modeling that renders real-time applications. Both approaches employ the direction-dependent quadratic approximation to construct their respective analytical inverse models. The first approach is viewed as an extension of the inverse model depicted by

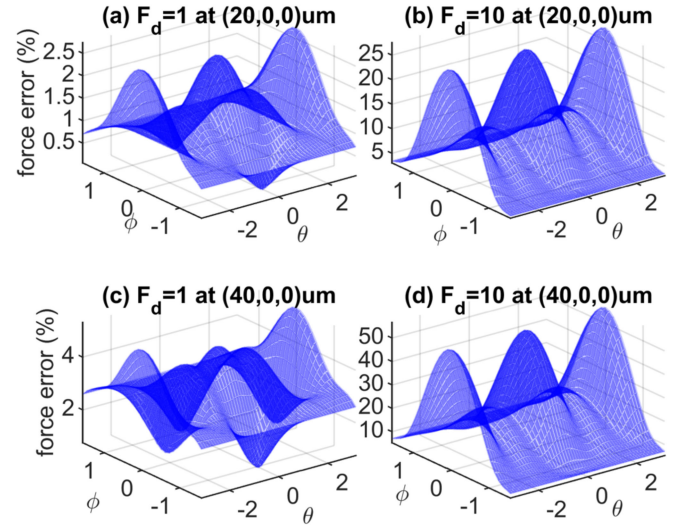


Fig. 4. Percent error of inverse modeling. (a) Bead at (20,0,0) μm , desired force $\hat{\mathbf{F}}_d = 1$. (b) Bead at (20,0,0) μm , desired force $\hat{\mathbf{F}}_d = 10$. (c) Bead at (40,0,0) μm , desired force $\hat{\mathbf{F}}_d = 1$. (d) Bead at (40,0,0) μm , desired force $\hat{\mathbf{F}}_d = 10$.

(5) in two fronts, i.e., based on the direction-dependent optimal current allocation at the center and using the second-order Taylor expansion in the spatial domain. The analytical inverse model is cast as the second order Taylor expansion for each individual current, i.e., $\hat{\mathbf{I}}_{\text{opt}}^{\text{unit}}(\varphi, \theta, \hat{\mathbf{p}})_i \approx \hat{\mathbf{I}}_{\text{opt}}^{\text{unit}}(\varphi, \theta)_i + \mathbf{G}_i(\varphi, \theta)\hat{\mathbf{p}} + \frac{1}{2}\hat{\mathbf{p}}^T \mathbf{H}_i(\varphi, \theta)\hat{\mathbf{p}}$, where $i = 1, 2, \dots, 6$ is the index of the six input currents, $\mathbf{G}_i(\varphi, \theta)$ the 3×1 gradient vector, and $\mathbf{H}_i(\varphi, \theta)$ the 3×3 hessian matrix [33]. Denoting $\mathcal{P} = [\hat{x}, \hat{y}, \hat{z}, 1]^T$ as the augmented position vector, the inverse model is expressed in the following quadratic form:

$$\hat{\mathbf{I}}_{\text{opt}}^{\text{unit}}(\varphi, \theta, \hat{\mathbf{p}})_i \approx \mathcal{P}^T \mathbf{D}_i^{\text{Taylor}}(\varphi, \theta) \mathcal{P} \quad (10)$$

where $\mathbf{D}_i^{\text{Taylor}}(\varphi, \theta)$ is the 4×4 inverse modeling matrix associated with the i th input current. It is constructed from $\hat{\mathbf{I}}_{\text{opt}}^{\text{unit}}(\varphi, \theta)_i$, $\mathbf{G}_i(\varphi, \theta)$, and $\mathbf{H}_i(\varphi, \theta)$ as follows:

$$\mathbf{D}_i^{\text{Taylor}} = \begin{bmatrix} \frac{1}{2}\mathbf{H}_i(\varphi, \theta) & \frac{1}{2}\mathbf{G}_i(\varphi, \theta) \\ \frac{1}{2}\mathbf{G}_i^T(\varphi, \theta) & \hat{\mathbf{I}}_{\text{opt}}^{\text{unit}}(\varphi, \theta)_i \end{bmatrix}. \quad (11)$$

The second approach starts with numerically finding the direction-dependent optimal current allocation at spatial positions predetermined in the 3-D workspace. Fig. 5 shows the selected spatial positions in the first Octant of the 3-D workspace, where $\hat{\mathbf{I}}_{\text{opt}}^{\text{unit}}(\varphi, \theta, \hat{\mathbf{p}})$ is numerically calculated using MATLAB optimization toolbox to minimize $J(\varphi, \theta, \hat{\mathbf{p}})$ in (7). The spatial range in the first Octant is a $45 \mu\text{m} \times 45 \mu\text{m} \times 45 \mu\text{m}$ cube. The least squares fitting is then employed to construct an analytical inverse model, wherein the format of (10) is kept for simplicity, i.e.

$$\hat{\mathbf{I}}_{\text{opt}}^{\text{unit}}(\varphi, \theta, \hat{\mathbf{p}})_i \approx \mathcal{P}^T \mathbf{D}_i^{LS}(\varphi, \theta) \mathcal{P}. \quad (12)$$

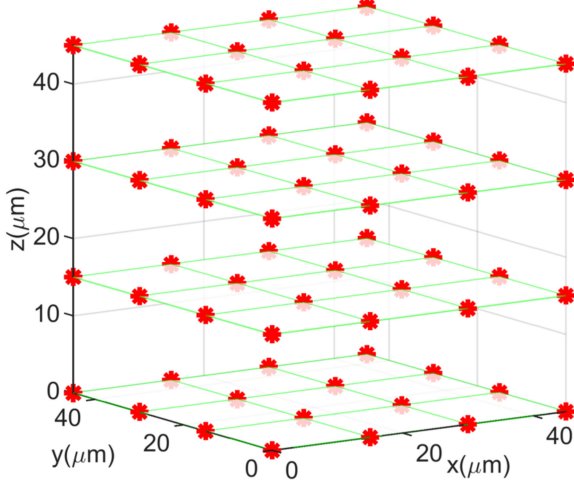


Fig. 5. Spatial positions where solutions of optimal current allocation are to be obtained.

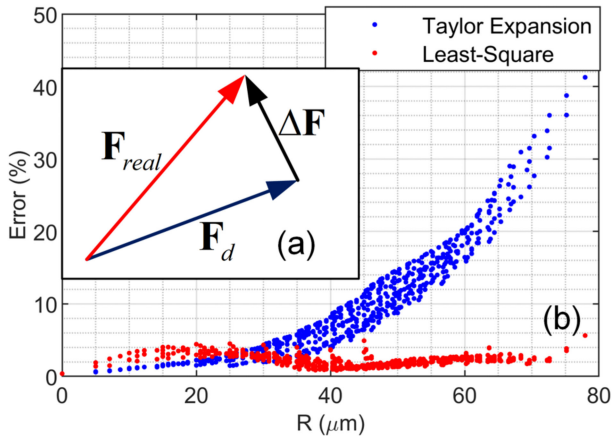


Fig. 6. Percent error of force production using the two inverse models.

The matrix $D_i^{LS}(\varphi, \theta)$ follows the same format of $D_i^{\text{Taylor}}(\varphi, \theta)$ in (10), but the entries of $D_i^{LS}(\varphi, \theta)$ are determined through the least squares fitting to minimize the 2-norm of the error within the specified 3-D spatial range.

To evaluate the accuracy of the inverse modeling, the error of the force production is examined at various positions within the $45 \mu\text{m} \times 45 \mu\text{m} \times 45 \mu\text{m}$ cube in the first Octant. At each position, the desired force (\mathbf{F}_d) is specified in numerous distinct directions. Each of the two inverse models is then applied to obtain the six input currents. The force model is then employed to calculate the real force (\mathbf{F}_{real}) produced by the actuation current. The percent error of the force production is shown in Fig. 6, wherein R is the distance from the center, i.e., $R = \|\mathbf{p}\|$, and the percent error is defined as $|\Delta\mathbf{F}/\mathbf{F}_d| \times 100$, referred to Fig. 6(a). The maximum force modeling error at each location is selected and plotted in Fig. 6(b). It can be clearly seen that the percent error grows with respect to R when using the Taylor expansion, whereas it remains under 5% in the case that the inverse model be constructed through the least squares fitting.

The optimal inverse modeling not only solves four difficulties in using multipole electromagnetic actuation, i.e., 1) coupling,

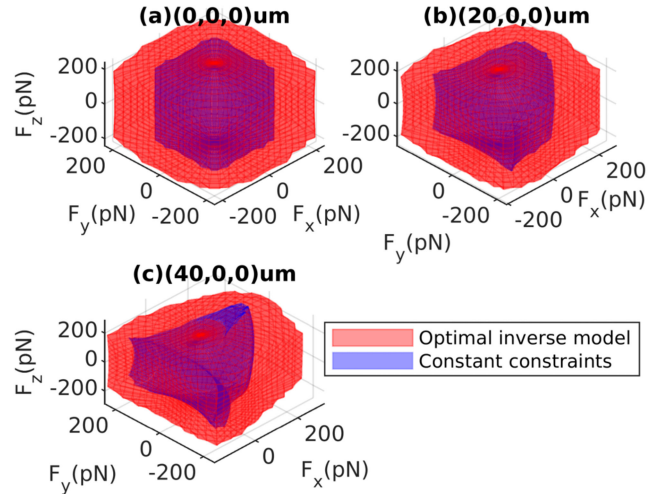


Fig. 7. Force production volumes (a) at $(0,0,0) \mu\text{m}$, (b) at $(20,0,0) \mu\text{m}$, and (c) at $(40,0,0) \mu\text{m}$.

2) redundancy, 3) nonlinearity, and 4) position-dependency but also significantly increases the capability of the force production, which is measured by the force production volume. Any desired force vector within the force production volume can be produced by the actuator under the limit specified for the input current. The capability with the current limitation being three amperes using the optimal inverse model [see (12)] and that using the inverse model based on constant constraints [see (5)] are compared in Fig. 7 at three distinct positions. It is seen that the capability of the force production is position-dependent and that the optimal inverse modeling significantly increases the size of the force production volume.

IV. 3-D MAGNETIC FORCE PRODUCTION IN HEXAPOLE ACTUATION

With the inverse modeling, i.e., (5) or (12), being implemented in a high-speed FPGA system, the real-time current allocation can be realized to make the hexapole actuating system behave like a decoupled three-axis force producer to enable the active control of the magnetic particle. Experimental investigations of the effective 3-D magnetic force production through the optimal current allocation are presented in this section.

A. Feedback Stabilization of Magnetic Trap

In the experiment, the hexapole actuating system is used to trap and move a magnetic particle in aqueous solutions. A block diagram of the feedback control system is shown in Fig. 8. It is worth noting that the objective of the control system implemented in the experiment is to examine the actuation current and to evaluate the force error from the point of view of the force production.

The dynamics of a microscopic bead moving in aqueous solutions is governed by the Langevin equation at low Reynolds numbers [34], driven by the controllable electromagnetic force \mathbf{F}_{MT} and subject to random thermal forces \mathbf{F}_T , i.e.

$$\gamma \dot{\mathbf{p}}(t) = \mathbf{F}_{\text{MT}}(\mathbf{p}(t), \mathbf{I}(t)) + \mathbf{F}_T(t) \quad (13)$$

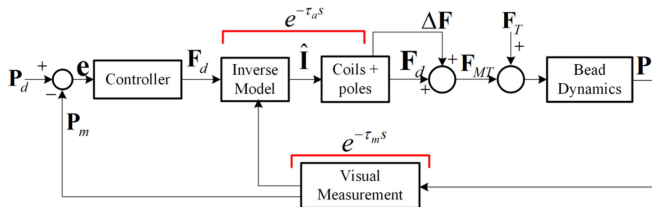


Fig. 8. Block diagram of the feedback control system: p_d is the desired position, p_m the measured position, e the error signal, F_d the desired force determined by the control law, τ_a the effective actuator delay, τ_m the measurement delay, F_{MT} the magnetic force, ΔF the error of force production, and F_T the thermal force.

where γ is the drag coefficient, characterized by Stokes' law, \mathbf{p} the position vector, and \mathbf{I} the input current vector. The total time delay (τ_D) of the feedback system is the combination of the actuator delay (τ_A), the measurement delay (τ_m), and the zero-order-hold delay (τ_{ZOH}), i.e., $\tau_D = \tau_A + \tau_m + \tau_{ZOH}$. Moreover, the effective actuator delay is denoted as τ_a , i.e., $\tau_a = \tau_A + \tau_{ZOH}$. Therefore, the bead dynamics is expressed as follows:

$$\gamma \dot{\mathbf{p}}(t) = \mathbf{F}_{MT}(\mathbf{p}(t), \mathbf{I}(\mathbf{F}_d(t), \mathbf{p}(t - \tau_m))) + \mathbf{F}_T(t) \quad (14)$$

wherein $\mathbf{I}(\mathbf{F}_d(t), \mathbf{p}(t - \tau_m))$ denotes the current allocation in real time. The input/output relationship of the feedback linearized actuator is cast as $\mathbf{F}_{MT} = \mathbf{F}_d + \Delta \mathbf{F}$, wherein $\Delta \mathbf{F}$ characterizes the error of the force production and is dictated by the error of force modeling and that of the inverse modeling. It is seen that when using the optimal current allocation to control the magnetic particle makes the dynamics of the feedback loop very simple and the stability of the control system is dictated by $\Delta \mathbf{F}$ and τ_D .

A proportional control law, i.e., $\mathbf{F}_d(t) = K_p(\mathbf{p}_d(t) - \mathbf{p}(t - \tau_m))$, along with the current allocation was realized and applied to achieve stabilization in experiments. Considering the effective actuator delay and the error of the modeling and of the inverse modeling, the equation of motion of the actively controlled bead is cast below

$$\gamma \dot{\mathbf{p}}(t) = K_p(\mathbf{p}_d(t - \tau_a) - \mathbf{p}(t - \tau_D)) + \Delta \mathbf{F}(t) + \mathbf{F}_T(t). \quad (15)$$

As the error of the force modeling could be significantly reduced through the experimental calibration [25], a great part of $\Delta \mathbf{F}$ is caused by the error of the inverse modeling. If constant constraints were being employed, as illustrated in Fig. 4, the error of the inverse modeling, and, thus, $\Delta \mathbf{F}$, is obvious. However, when using the optimal inverse modeling, the error of the force production $\Delta \mathbf{F}$ could be significantly smaller, as shown in Fig. 6.

Therefore, with the proposed optimal current allocation, the stability of the feedback loop is practically dictated by the time delay of the feedback loop. The characteristic equation of the simplified continuous-time feedback loop is cast as follows:

$$1 + \frac{K_p e^{-\tau_D s}}{\gamma s} = 0. \quad (16)$$

The Nyquist stability criterion requires that K_p be smaller than $\pi/\sqrt{2\tau_D}$. When implementing the controller in digital form,

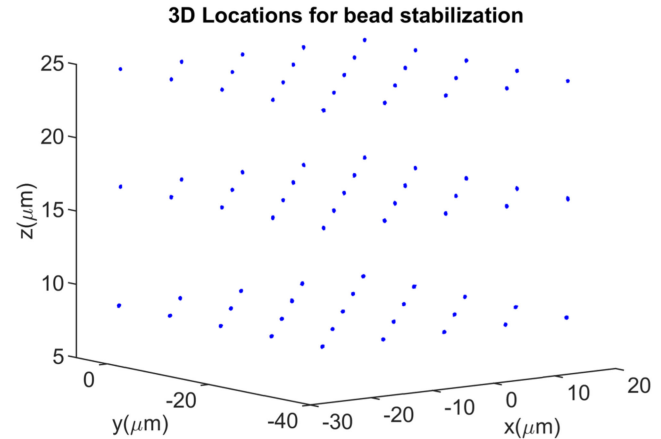


Fig. 9. Magnetic bead is moved to and stabilized at 75 distinct positions, distributed in three planes at distinct z height, in the 3-D workspace (result using optimal current allocation).

wherein the measurement delay equals to two sampling periods of the control system being considered, i.e., $\tau_D = 2T$, the characteristic equation of the discrete system is as follows:

$$1 + K_p z^{-2} \frac{\frac{T}{\gamma}}{z - 1} = 0 \quad (17)$$

wherein z^{-2} is attributed to the two-step measurement delay and $T/\gamma(z - 1)$ the discrete model of the digital-to-analog converter combined with the bead dynamics. The stability range can be determined through Jury's stability test [35], i.e.,

$$0 < K_p < \frac{-1 + \sqrt{5}}{2} \frac{\gamma}{T} \cong 0.618 \frac{\gamma}{T}. \quad (18)$$

It is worth noting that the simplicity in the stability analysis is attributed to the optimal inverse modeling, which solves the four major challenges in the current allocation and achieves the accurate force production.

B. Actuation Current and Force Error

In case the stabilized positioning $\mathbf{p}_d(t)$ is constant and the steady-state error of positioning, denoted as \mathbf{e}_{ss} , is inversely proportional to the control gain employed, i.e., $\mathbf{e}_{ss} = -\Delta \mathbf{F}/K_p$, it is seen that the steady-state positioning error serves as a quantitative measure of $\Delta \mathbf{F}$, indicating the error of modeling and of inverse modeling.

In the experiment of the stabilized positioning, the magnetic bead is moved to and stabilized at 75 distinct positions, distributed in three planes, in the 3-D workspace, as shown in Fig. 9. The magnetic bead is stabilized at each point for 10 s, and then steered at 5 $\mu\text{m}/\text{s}$ by 10 μm to the next point. It is first stabilized at the lower left corner and steered to follow a zigzag path until reaching the last point in the plane. It is then steered back to the starting point and moved to the first point in the next plane. After the transient response vanished at each position, the input current and the bead position associated with the last 7 s were selected, analyzed, and plotted.

The current allocation based on the optimal inverse modeling and that using constant constraints were implemented at a sampling rate of 1606 Hz. The value of the control gain was selected

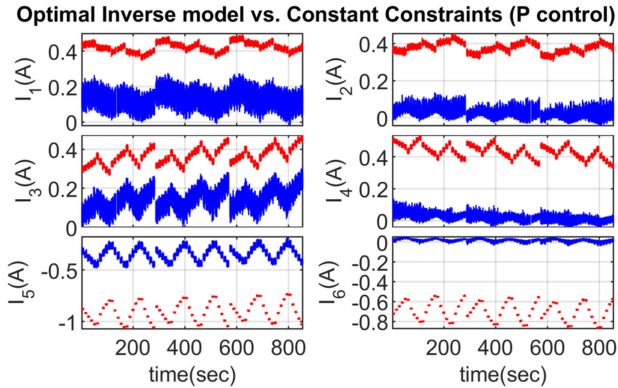


Fig. 10. Actuation current for positioning: based on optimal inverse modeling (blue) and using constant constraints (red).

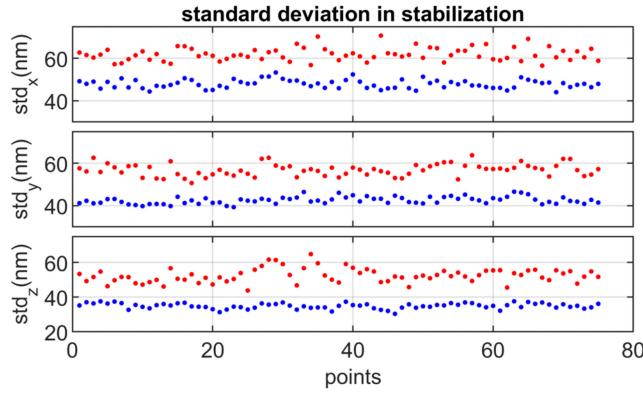


Fig. 11. Standard deviation of Brownian motion: based on optimal inverse modeling (blue) and using constant constraints (red).

to be half of the stability limit. Fig. 10 compares the actuation current of the two approaches employed in the experiment. It is seen that the current allocation based on the optimal inverse modeling requires significantly smaller actuation current than that using constant constraints. It is worth mentioning that I_5 and I_6 are negative when using constant constraints, but they have much larger absolute values when compared with the result based on the optimal inverse modeling.

The standard deviation of the bead's Brownian motion at each stabilized position was calculated and shown in Fig. 11. It is seen that the current allocation based on the optimal inverse modeling achieves superior Brownian motion control than that using constant constraints. It is worth noting that the current allocation using constant constraints results in larger actuation current, leading to greater error of force production and thus greater positioning fluctuation.

The positioning error of the bead is shown in Fig. 12. It is seen that the current allocation based on the optimal inverse modeling results in much smaller positioning errors. Since the steady-state error of positioning is inversely proportional to the control gain employed, i.e., $e_{ss} = -\Delta F/K_p$, the experimental result validates that the current allocation based on the optimal inverse modeling leads to smaller ΔF , which is attributed to the error of modeling and of inverse modeling.

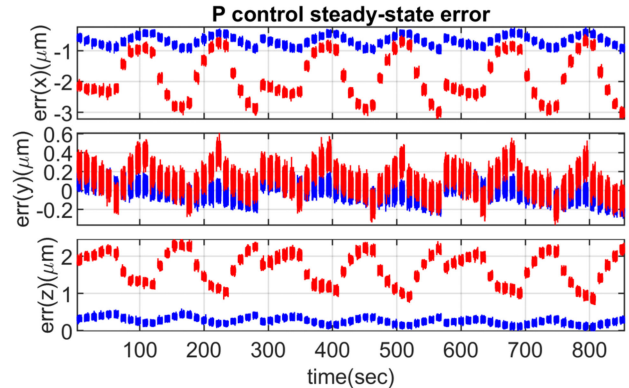


Fig. 12. Positioning error: based on optimal inverse modeling (blue) and using constant constraints (red).

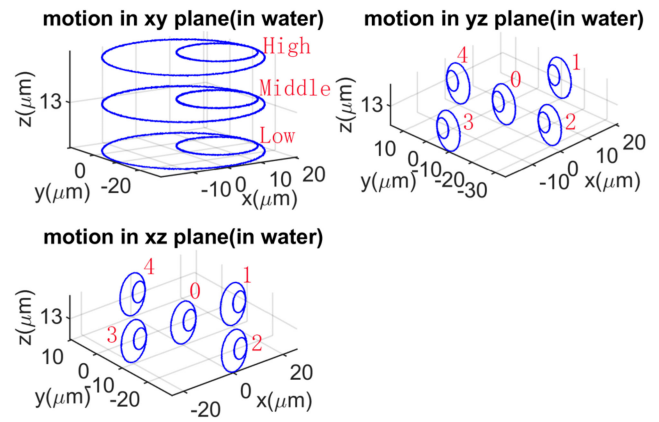


Fig. 13. Trajectory tracking in the 3-D workspace.

C. Actuation Current and Motion Error

A PI controller is implemented to render motion control to further validate the effectiveness of the proposed inverse modeling. In the experiment, the optimal current allocation along with the linear controller is applied to control the moving bead at different regions and along distinct directions. The ability to steer the magnetic bead in the workspace is necessary if it is to be used as a scanning probe.

In the experiment, the magnetic bead is steered at 5 $\mu\text{m}/\text{s}$ to track various circular trajectories, i.e., three in the xy -plane at distinct positions, five in the yz -plane at distinct positions, and five in the xz -plane at distinct positions. The bead is first steered to track the circle ($D = 40 \mu\text{m}$) in the lowest the xy -plane, then moved to the middle plane, being 5 μm above. After tracking the circle in the middle plane, the bead is moved to the highest plane to track the circular trajectory. After that, it is moved back to the middle plane and steered to track the circular trajectory ($D = 10 \mu\text{m}$) labeled as 0 in the xz -plane and the other one labeled as 0 in the yz -plane. It is worth mentioning that the circular trajectories in the yz -plane and the xz -plane are plotted separately in Fig. 13 for clarity, whereas the sequence of trajectory tracking is alternating between the yz -plane and the xz -plane, following the trajectory label of 0, 1, 2, 3, 4.

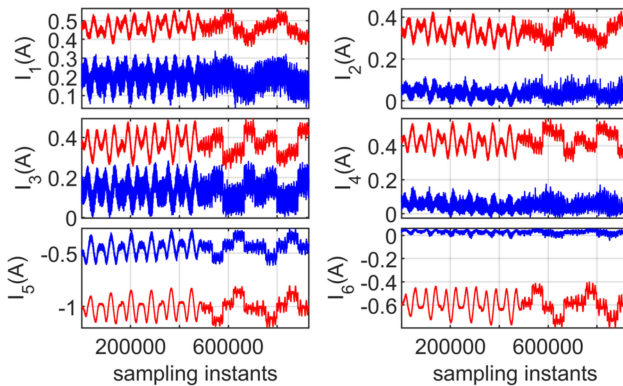


Fig. 14. Actuation current for trajectory tracking: based on optimal inverse modeling (blue) and using constant constraints (red).

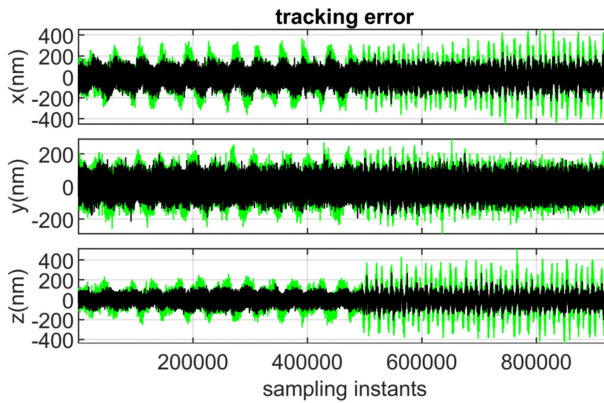


Fig. 15. Tracking error in three axes: based on optimal inverse modeling (black) and using constant constraints (green).

It is seen from Fig. 14 that the current allocation based on the optimal inverse modeling requires significantly smaller actuation currents to perform the 3-D trajectory tracking, which is as expected. Moreover, it results in much smaller tracking errors, which is shown in Fig. 15. It is worth noting that the bead is constantly under the excitation of the random thermal force $\mathbf{F}_T(t)$. Therefore, the Brownian motion is a significant component of the tracking error depicted in Fig. 15, wherein the mean of the tracking error is relatively small as a PI controller is employed. It is seen that by using the optimal inverse modeling to realize the current allocation, the standard deviation of the Brownian motion reduced to (57.82, 43.81, and 42.01 nm) from (123.10, 63.08, and 109.83 nm).

V. CONCLUSION

A current allocation scheme based on the optimal inverse modeling of hexapole electromagnetic actuation is devised through the numerical optimization and least squares fitting, realized in a high-speed FPGA system for the real-time current allocation rendering 3-D magnetic force production, and validated through experimental investigations. It solves the following four main difficulties in the multipole electromagnetic actuation:

- 1) redundancy;
- 2) coupling;

- 3) nonlinearity;
- 4) position-dependency.

It makes the six-input hexapole actuating system behave like a three-axis force producer to enable applications in active control.

Since optimal current allocation is able to minimize the 2-norm of the 6×1 input current vector when applied to produce the desired 3-D magnetic force, it greatly increases the capability of the force production of the actuator, theoretically demonstrated through using the force production volume to serve a quantitative measure. Compared with the current allocation using constant constraints, the scheme based on the optimal inverse modeling significantly reduces the error of the force production, which is demonstrated theoretically and experimentally.

Specifically, the stabilized positioning and trajectory tracking were experimentally investigated to show that compared to the current allocation using constant constraints, the optimal current allocation required significantly smaller actuation currents, achieved the superior Brownian motion control, and resulted in much smaller errors when applied to realize the active control for positioning and tracking.

There are still several aspects that need to be investigated to improve the capability of the magnetic actuator and to enhance the control of the magnetic bead to serve as a scanning probe. First, a Hall effect sensor needs to be integrated to each individual magnetic pole to provide the feedback signal to reduce the effect of hysteresis and other modeling error. Second, advanced control laws could be designed and implemented to realize more advanced applications, such as the rapid steering and controlled manipulation. In case that the probe is to interact with samples or environment, it is necessary to estimate in real time the probe–sample interaction or the spatially dependent physical quantities to enable the self-tuning adaptive control. Specifically, the spatial-dependent parameter, such as drag coefficient, needs to be estimated in real time to enhance the control of the moving probe. Moreover, the real-time estimation of the probe–sample interaction needs to be realized to enable the automatic scanning.

REFERENCES

- [1] C. Haber and D. Wirtz, "Magnetic tweezers for DNA micromanipulation," *Rev. Sci. Instrum.*, vol. 71, no. 12, pp. 4561–4570, 2000.
- [2] J. Zlatanova and S. H. Leuba, "Magnetic tweezers: A sensitive tool to study DNA and chromatin at the single-molecule level," *Biochem. Cell Biol.*, vol. 81, pp. 151–159, 2003.
- [3] C.-H. Chiou, Y.-Y. Huang, M.-H. Chiang, H.-H. Lee, and G.-B. Lee, "New magnetic tweezers for investigation the mechanical properties of single DNA molecules," *Nanotechnology*, vol. 17, pp. 1217–1224, 2006.
- [4] J. K. Fisher *et al.*, "Thin-foil magnetic force system for high-numerical-aperture microscopy," *Rev. Sci. Instrum.*, vol. 77, 2006, Art. no. 023702.
- [5] J.-A. Seon, Z. Cenev, and Q. Zhou, "Automatic noncontact extraction and independent manipulation of magnetic particles using electromagnetic needle," *IEEE/ASME Trans. Mechatron.*, vol. 25, no. 2, pp. 931–941, Apr. 2020.
- [6] A. R. Bausch, F. Ziemann, A. A. boulbitch, K. Jacobson, and E. Sackmann, "Local measurements of viscoelastic parameters of adherent cell surfaces by magnetic bead microrheometry," *Biophys. J.*, vol. 76, pp. 2038–2049, Oct. 1998.
- [7] F. J. Alenghat, B. Fabry, K. Y. Tsai, W. H. Goldmann, and D. E. Ingber, "Analysis of cell mechanics in single vinculin-deficient cells using a magnetic tweezer," *Biochem. Biophys. Res. Commun.*, vol. 277, pp. 93–99, 2000.

- [8] H. Huang, C. Y. Dong, H.-S. Kwon, J. D. Sutin, R. D. Kamm, and P. T. C. So, "Three-dimensional cellular deformation analysis with a two-photon magnetic manipulator workstation," *Biophys. J.*, vol. 82, pp. 2211–2223, 2002.
- [9] A. R. Bausch, W. Moller, and E. Sackmann, "Measurement of local viscoelasticity and forces in living cells by magnetic tweezers," *Biophys. J.*, vol. 76, pp. 573–579, 1999.
- [10] B. G. Hosu, K. Jakab, P. Banki, and F. I. Toth, "Magnetic tweezers for intracellular applications," *Rev. Sci. Instrum.*, vol. 74, no. 9, pp. 4158–4163, 2003.
- [11] A. H. B. de Vries, B. E. Krenn, R. van Driel, and J. S. Kanger, "Micro magnetic tweezers for nanomanipulation inside live cells," *Biophys J.*, vol. 88, no. 3, pp. 2137–2144, 2005.
- [12] J. S. Kanger, V. Subramaniam, and R. van Driel, "Intracellular manipulation of chromatin using magnetic nanoparticles," *Chromosome Res.*, 16, pp. 511–522, 2008.
- [13] T. Honda, K.I. Arai, and K. Ishiyama, "Micro swimming mechanisms propelled by external magnetic fields," *IEEE Trans. Magn.*, vol. 32, no. 5, pp. 5085–5087, Sep. 1996.
- [14] L. Zhang, J. J. Abbott, L. X. Dong, B. E. Kratochvil, D. Bell, and B. J. Nelson, "Artificial bacterial flagella: Fabrication and magnetic control," *Appl. Phys. Lett.*, vol. 94, 2009, Art. no. 064107.
- [15] J. Yu and L. Zhang, "Reversible swelling and shrinking of paramagnetic nanoparticle swarms in biofluids with high ionic strength," *IEEE/ASME Trans. Mechatron.*, vol. 24, no. 1, pp. 154–163, Feb. 2019.
- [16] M. P. Kumar, J. J. Abbott, B. E. Kratochvil, R. Borer, A. Sengul, and B. J. Nelson, "OctoMag: An electromagnetic system for 5-DOF wireless micromanipulation," *IEEE Trans. Robot.*, vol. 26, no. 6, pp. 1006–1017, Dec. 2010.
- [17] C. Bergeles, B. E. Kratochvil, and B. J. Nelson, "Visually servoing magnetic intraocular microdevices," *IEEE Trans. Robot.*, vol. 28, no. 4, pp. 798–809, Aug. 2012.
- [18] Z. Zhang, K. Huang, and C.-H. Menq, "Design, implementation, and force modeling of quadrupole magnetic tweezers," *ASME/IEEE Trans. Mechatron.*, vol. 15, no. 5, pp. 704–713, Oct. 2010.
- [19] Z. Zhang and C.-H. Menq, "Design and modeling of a 3-D magnetic actuator for magnetic microbead manipulation," *IEEE/ASME Trans. Mechatron.*, vol. 16, no. 3, pp. 421–430, Jun. 2011.
- [20] S. Earnshaw, "On the nature of the molecular forces which regulate the constitution of the luminiferous ether," *Trans. Camb. Phil. Soc.*, vol. 7, pp. 97–112, 1842.
- [21] Z. Zhang and C.-H. Menq, "Three-dimensional particle tracking with subnanometer resolution using off-focus images," *Appl. Opt.*, vol. 47, no. 14, pp. 2361–2370, 2008.
- [22] Z. Zhang, Y. Huang, and C.-H. Menq, "Actively controlled manipulation of a magnetic microbead using quadrupole magnetic tweezers," *IEEE Trans. Robot.*, vol. 26, no. 3, pp. 531–541, Jun. 2010.
- [23] Z. Zhang, F. Long, and C.-H. Menq, "Three-dimensional visual servo control of a magnetically propelled microscopic bead," *IEEE Trans. Robot.*, vol. 29, no. 2, pp. 373–382, Apr. 2013.
- [24] Z. Zhang, Y. Shi, S. M. Jhiang, and C.-H. Menq, "Mechanical anisotropy and adaptation of metastatic cells probed by magnetic microbeads," in *Proc. Imag., Manipulat., Anal. Biomolecules, Cells, Tissues VIII*, vol. 7568, San Francisco, CA, USA, Feb. 2010. [Online]. Available: <https://doi.org/10.1117/12.842086>
- [25] F. Long, D. Matsuura, and C.-H. Menq, "Actively controlled hexapole electromagnetic actuating system enabling 3-D force manipulation in aqueous solutions," *IEEE/ASME Trans. Mechatron.*, vol. 21, no. 3, pp. 1540–1551, Jun. 2016.
- [26] P. Mörters and Y. Peres, *Brownian Motion*. Cambridge, U.K.: Cambridge Univ. Press, Apr. 2010.
- [27] Y. Huang, Z. Zhang, and C.-H. Menq, "Minimum-variance Brownian motion control of an optically trapped probe," *Appl. Opt.*, vol. 48, pp. 5871–5880, 2009.
- [28] P. Cheng, S. M. Jhiang, and C. H. Menq, "Real-time visual sensing system achieving high-speed 3D particle tracking with nanometer resolution," *Appl. Opt.*, vol. 52, no. 31, pp. 7530–7539, Nov. 2013.
- [29] B. M. Lansdorp, S. J. Tabrizi, A. Dittmore, and O. A. Saleh, "A high-speed magnetic tweezer beyond 10,000 frames per second," *Rev. Sci. Instrum.*, vol. 84, no. 4, Apr. 2013.
- [30] P. Cheng and C. H. Menq, "Real-time continuous image registration enabling ultra-precise two-dimensional motion tracking," *IEEE Trans. Image Process.*, vol. 22, no. 5, pp. 2081–2090, May 2013.
- [31] P. Cheng and C. H. Menq, "Visual tracking of six-axis motion rendering ultraprecise visual servoing of microscopic objects," *IEEE/ASME Trans. Mechatron.*, vol. 23, no. 4, pp. 1564–1572, Aug. 2018.
- [32] R. T. Rockafellar, "Lagrange multipliers and optimality," *SIAM Rev.*, vol. 35, pp. 183–238, 1993.
- [33] W. C. Thacker, "The role of the Hessian matrix in fitting models to measurements," *J. Geophys. Res., Oceans*, vol. 94, pp. 6177–6196, 1989.
- [34] W. Coffey, Y. P. Kalmykov, and J. Waldron, *The Langevin Equation: With Applications to Stochastic Problems in Physics in Chemistry and Electrical Engineering*, 2nd ed., Singapore: World Scientific Publishing Company, 2004.
- [35] G. F. Franklin, J. D. Powell, and M. Workman, *Digital Control of Dynamic Systems*, 3rd ed., Menlo Park, CA, USA: Addison-Wesley, 1998.



Fei Long received the B.S. degree from Shanghai Jiao Tong University, Shanghai, China, in 2009, and the Ph.D. degree from The Ohio State University, Columbus, OH, USA, in 2016, both in mechanical engineering.

Currently, he is with the UBTECH Robotics North America Research and Development Center, Shenzhen, China, as a Staff Engineer. His research interests include modeling, control, and sensing of electro-mechanical systems, robot motion control, and motion planning.



Peng Cheng received the B.S. degree in theory and applied mechanics and the Ph.D. degree in solid mechanics from the University of Science and Technology of China, Hefei, China, in 2002 and 2007, respectively.

He is currently a Research Associate with The Ohio State University, Columbus, OH, USA. His primary research interests include optical metrology, microscopic imaging and image analysis, and visual-sensing-based real-time high-speed multi-DOF motion tracking.



Ta-Min Meng received the B.S. degree in power mechanical engineering from the National Tsing Hua University, Hsinchu, Taiwan, in 2015. He is currently working toward the Ph.D. degree in modeling and control of electromagnetic actuation with the Department of Mechanical and Aerospace Engineering, The Ohio State University, Columbus, OH, USA.

His research interests include modeling, control, and estimation of precision electromechanical systems.



Chia-Hsiang Menq received the Ph.D. degree in mechanical engineering from Carnegie Mellon University, Pittsburgh, PA, USA, in 1985.

Since 1985, he has been with the Ohio State University, where he is currently Professor and Ralph W. Kurtz Endowed Chair in Mechanical Engineering. His research has four areas of focus; control, sensing, and instrumentation; metrology, precision engineering, and manufacturing; imaging and mechanical characterization of live cells; and visual sensing and visual servo

control.

Prof. Menq has been the holder of the Ralph W. Kurtz Endowed Chair in Mechanical Engineering with The Ohio State University since 2006. He is a Fellow of the American Society of Mechanical Engineers (ASME), the Association for the Advancement of Science (AAAS), and the Society of Manufacturing Engineers (SME).